EES Solar

Accepted Manuscript

This article can be cited before page numbers have been issued, to do this please use: D. Ma, K. K. Bhowmik, L. Zhu, A. Ievlev, Y. Liu and L. Zhao, *EES Sol.*, 2026, DOI: 10.1039/D6EL00062B.

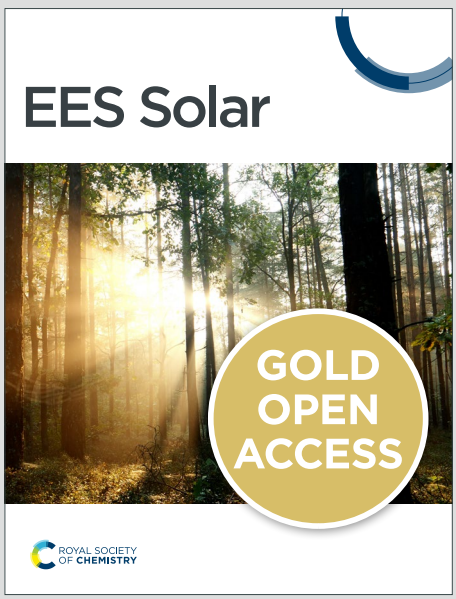

View Article Online
DOI: 10.1039/D6EL00062B

Broader Context

Perovskite solar cells are approaching performance levels relevant to large-scale deployment, but scale-up requires fabrication steps that do not quietly damage the active layer. Vacuum thermal evaporation is widely used to deposit charge-transport and metal contact layers in high-efficiency single-junction and tandem devices because it offers conformal coverage and precise thickness control. Our work shows that this useful process can also impose an underappreciated radiative stress that destabilizes the perovskite surface before the device is completed. By directly capturing iodine-containing volatile species and tracking the associated interfacial energetic reconstruction, we show how a common fabrication step can create hidden recombination losses and shorter device lifetime. We also demonstrate that a simple L-ascorbic-acid surface treatment can suppress this damage pathway. These findings highlight process compatibility as a central challenge for scalable photovoltaic manufacturing and suggest that chemically protecting the perovskite interfaces could improve yield, reproducibility, and durability in next-generation solar technologies.

View Article Online
DOI: 10.1039/D6EL00062B

Suppressing Thermal Evaporation-Induced Iodine Outgassing and Interfacial Degradation in Perovskite Solar Cells

Danqing Ma[1], Kanak Kanti Bhowmik[1], Lin Zhu[1], Anton Ievlev[2], Yongtao Liu[2], Lianfeng Zhao[1,]*

[1]Holcombe Department of Electrical and Computer Engineering, Clemson University, Clemson, South Carolina 29634, United States

[2]Center for Nanophase Materials Sciences, Oak Ridge National Laboratory, Oak Ridge, TN, 37830, United States

[*]Email: Lianfez@clemson.edu

View Article Online
DOI: 10.1039/D6EL00062B

Abstract

Vacuum thermal evaporation is widely used to deposit buffer layers and metal electrodes in perovskite solar cells, but the associated thermal radiation can damage the perovskite surface before the device stack is completed. Here we show that, under practical evaporation conditions, this hidden process stress drives near-surface degradation at the perovskite interface, leading to grain-boundary-localized morphological weakening and a shift in surface energetics toward a higher-work-function, more electron-deficient near-surface state. By integrating an Ag-mesh trapping experiment with X-ray photoelectron spectroscopy, we directly verify iodine outgassing from irradiated films. An L-ascorbic acid (LAA) surface treatment suppresses iodine volatilization, largely preserves the surface energetic landscape, and mitigates the associated solar cell degradation. These results move beyond simply recognizing evaporation-induced damage by identifying a chemically addressable interface-degradation mechanism and a practical strategy for protecting scalable perovskite solar cell fabrication.

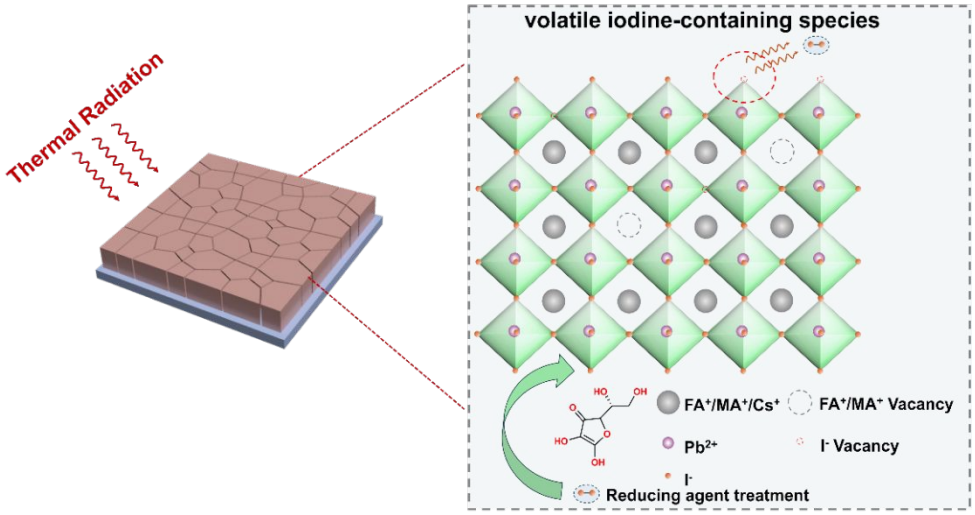

View Article Online
DOI: 10.1039/D6EL00062B

Broader Context

Perovskite solar cells are approaching performance levels relevant to large-scale deployment, but scale-up requires fabrication steps that do not quietly damage the active layer. Vacuum thermal evaporation is widely used to deposit charge-transport and metal contact layers in high-efficiency single-junction and tandem devices because it offers conformal coverage and precise thickness control. Our work shows that this useful process can also impose an underappreciated radiative stress that destabilizes the perovskite surface before the device is completed. By directly capturing iodine-containing volatile species and tracking the associated interfacial energetic reconstruction, we show how a common fabrication step can create hidden recombination losses and shorter device lifetime. We also demonstrate that a simple L-ascorbic-acid surface treatment can suppress this damage pathway. These findings highlight process compatibility as a central challenge for scalable photovoltaic manufacturing and suggest that chemically protecting the perovskite interfaces could improve yield, reproducibility, and durability in next-generation solar technologies.

Introduction

Metal halide perovskite solar cells have reached power conversion efficiencies (PCEs) approaching commercial relevance owing to their low-temperature processability, strong light absorption, long carrier diffusion lengths, and notable defect tolerance.[1–3] However, transitioning from high-performing laboratory cells to commercial modules requires exceptional long-term operational stability.[4–6] Understanding how and why these materials degrade is therefore one of the defining scientific challenges in the field. Most prior work on perovskite stability has focused on the operational lifetime of finished devices, correlating performance loss with environmental

View Article Online
DOI: 10.1039/D6EL00062B

stressors such as moisture, oxygen, heat, illumination, and electrical bias.[7,8] That body of work has been essential, but it leaves a major blind spot. By the time a device enters operation, the perovskite has already experienced a complex sequence of thermal, vacuum, chemical, and interfacial perturbations during fabrication, such as the stressors in the process of the buffer layer and electrode deposition by vacuum thermal evaporation. In soft ionic semiconductors such as halide perovskites, where ions are mobile, defect formation energies are comparatively low, and interfaces strongly influence electronic behavior, those processing environments can establish the initial defect density, near-surface stoichiometry, interface chemistry, and metastable state of the material. In other words, part of what is often labeled as "operational degradation" may already be encoded during manufacturing.

In perovskite solar cells, vacuum thermal evaporation is a core manufacturing step for depositing buffer layers and metal contacts. This route is attractive because it offers conformal coverage, accurate thickness control, and compatibility with multilayer device integration. While macroscopic thermal degradation of perovskite solar cells from environmental heat has been widely documented,[9–17] the impact of thermal radiation emitted directly from evaporation sources onto the underlying perovskite remains poorly understood. In fact, the vacuum thermal evaporation process that is generally treated as a passive finishing step may instead impose a damaging stress on the perovskite surface. Previous studies have shown that thermal stress can drive the oxidation of lattice iodide into molecular iodine and related iodine species.[18] Recent work further suggests that thermal radiation during vacuum processing can aggravate this iodine loss from perovskite surfaces.[19] However, the electronic consequences of this process—which directly dictate non-radiative recombination and open-circuit voltage losses—remain largely unexplored.

View Article Online
DOI: 10.1039/D6EL00062B

In this work, we systematically investigate the degradation induced by thermal radiation during vacuum evaporation and demonstrate a chemical strategy to mitigate it. By integrating an *in-situ* Ag-mesh trapping experiment, we directly capture and verify the release of volatile iodine-containing species. We show that source-generated thermal radiation drives this near-surface chemical loss, along with grain-boundary-localized morphological weakening and a coupled reconstruction of the perovskite interface energetic landscape. We further demonstrate that an L-ascorbic acid (LAA, **Figure S1a**, Supporting Information) surface treatment suppresses this degradation pathway and improves device robustness. Together, these results show that vacuum evaporation is not merely a passive finishing step, but a chemically consequential stage that can be actively engineered in scalable perovskite solar cell processing.

Results and Discussion

To determine whether thermal evaporation introduces hidden interfacial damage, we first established the baseline inverted architecture shown in **Figure 1a** (ITO/MeO-2PACz/perovskite/C_{60}/BCP/Ag), in which the upper layers of C_{60}, BCP and Ag were deposited by thermal evaporation. We then used a wash-and-peel-off method (see the Method section for details) to expose the perovskite surface after overlayer deposition (**Figures 1b and 1c**). Spatially resolved 2D PL lifetime maps of the exposed films (**Figures 1d–1f**) reveal a progressive lifetime reduction as the number of evaporation steps increases, indicating an accumulation of non-radiative recombination centers near the top perovskite surface.[20] To further prove the degradation is induced by thermal evaporation rather than the wash-and-peel-off method, we also studied a bare perovskite film before and after the chlorobenzene washing treatment. The average lifetime changes only slightly from 25.78 to 24.32 ns after chlorobenzene washing, and the corresponding

View Article Online
DOI: 10.1039/D6EL00062B

two-dimensional PL lifetime maps remain relatively uniform (**Figure S2** and **Table S1**, Supporting Information). Therefore, the pronounced lifetime loss observed after evaporated-layer deposition and removal is attributed primarily to evaporation/radiation-induced interfacial degradation rather than to the washing step itself.

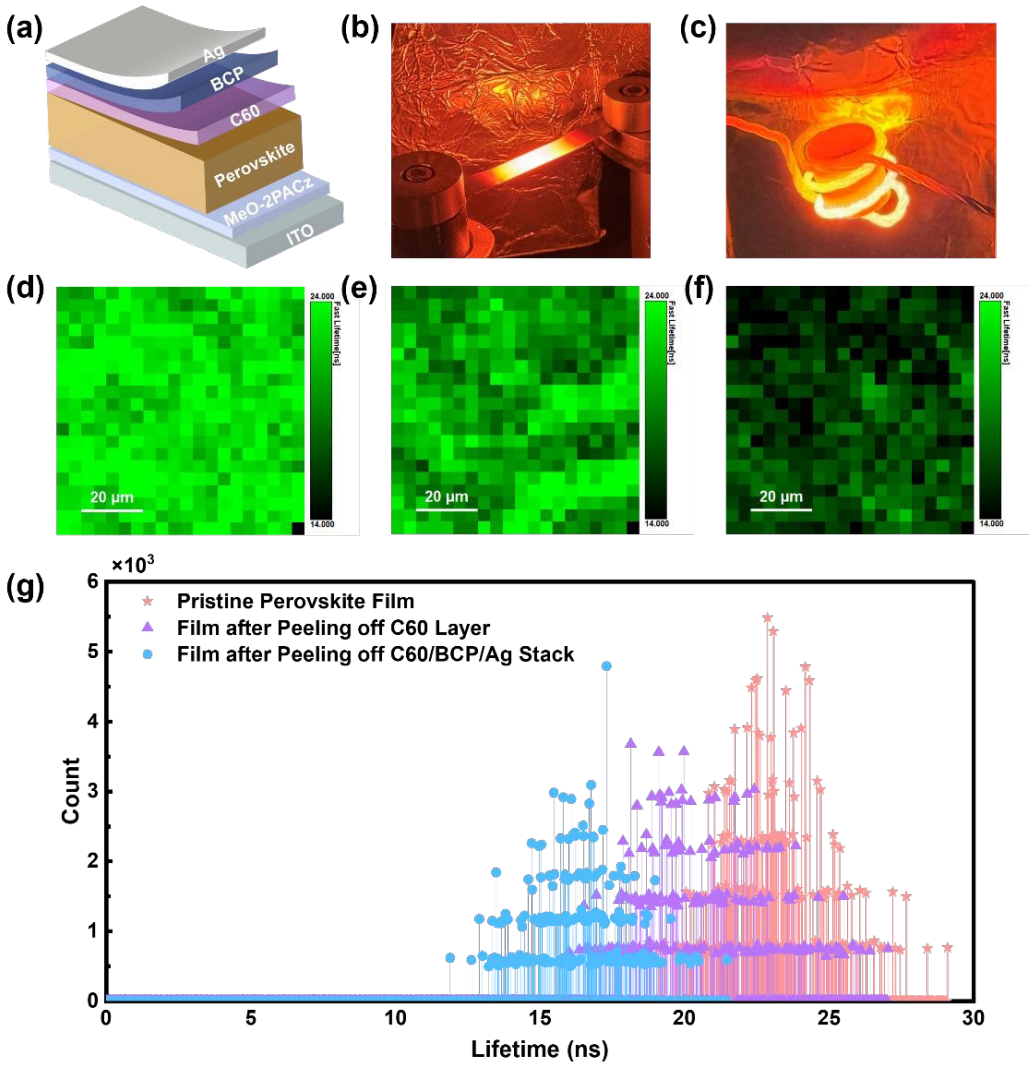

Figure 1. Overview of device architecture, fabrication, and optical mapping. **(a)** Schematic representation of the planar p-i-n perovskite solar cell structure (ITO/MeO-2PACz/Perovskite/ C_{60}/BCP/Ag). **(b)** and **(c)** Photographs capturing the thermal evaporation processes for Ag deposition from an Ag boat (b) and C_{60} deposition from a C_{60} boat (c). **(d–f)** Two-dimensional

View Article Online
DOI: 10.1039/D6EL00062B

photoluminescence (2D PL) lifetime mapping of perovskite films: (d) Pristine perovskite film. (e) Perovskite film after removing the C_{60} layer. (f) Perovskite film after removing the C_{60}/BCP/Ag stack. **(g)** Histogram distributions of the average PL lifetime for the films shown in panels d–f.

To verify the device-level impact of this processing step and to separate the effect of high vacuum from that of source-generated thermal radiation, we compared pristine samples with samples held in vacuum for 30 min and samples exposed to thermal radiation for the same duration (**Figure S3** and **S4,** and **Table S2**, Supporting Information). Under the exposure conditions used here, holding the films in high vacuum for 30 min produced only minor changes, whereas source-generated thermal radiation caused clear performance losses, most notably in open-circuit voltage (V_{oc}) and fill-factor (*FF*). This trend is consistent with the PL lifetime distributions in **Figure 1g**, which shift progressively to shorter lifetimes from the pristine film to the C_{60}-removed film and then to the full-stack-removed film. Because the damage is created at the perovskite/electron-selective interface, such voltage and *FF* penalties are consistent with increased interfacial non-radiative recombination and less favorable charge extraction. Together, these results identify source-generated thermal radiation as the dominant driver of evaporation-induced interfacial degradation in the present experiments.

To further isolate the thermal radiation component from the complex vacuum thermal evaporation environment, we simulated the evaporation environment using an empty Ag boat operated at 93.9 W (2.64 V, 35.6 A), *i.e.*, the same electrical conditions used during Ag deposition but without depositing material. Microscopy surveys reveal that this radiation induces distinct morphological deterioration. Before thermal radiation exposure, the pristine film exhibits a compact and continuous polycrystalline surface in SEM (**Figures 2a,b**). After radiation, SEM reveals grain-boundary-localized pinhole-like defects and local surface discontinuities (**Figures 2c,d**),

View Article Online
DOI: 10.1039/D6EL00062B

indicating localized structural weakening near the surface.[21–23] AFM does not resolve comparably pronounced pinhole-like features; instead, the irradiated surface shows roughened topography with shallow depressions and a locally pitted/porous, partially cellular texture in the enlarged image (**Figures 2g,h**). One possible reason is that thermal radiation first produces a weakened, partially voided intergranular morphology, which AFM captures as pitted or porous depressions, while SEM accentuates these vulnerable regions as pinhole-like defects because beam-sensitive perovskites may undergo additional volatilization under vacuum/e-beam exposure. [24,25]

Because this morphological degradation is strongly localized at the grain boundaries, we hypothesized that the density of grain boundaries should dictate the severity of optoelectronic damage. To test this, we examined bare perovskite films prepared from precursor solutions of 1.5, 1.25, and 1.0 M. As established in previous studies, lower precursor concentrations yield thinner perovskite films with correspondingly smaller average grain sizes, thereby inherently possessing a higher density of grain boundaries per unit area.[26] Time-resolved photoluminescence (TRPL) measurements confirm this grain-boundary-mediated degradation. As shown in **Figures 2i–k**, the TRPL decays exhibit a clear thickness dependence after 30 min of thermal-radiation exposure. The average carrier lifetime of the 1.5 M film decreases from 29.58 to 23.12 ns (an attenuation of 21.86%). In contrast, the 1.25 M and 1.0 M films show much more severe attenuation rates of 35.34% and 39.24%, respectively (**Table S3**, Supporting Information). The higher density of radiation-induced defective grain boundaries in the thinner films acts as a sink for diffusing carriers, which accounts for the accelerated non-radiative recombination and lifetime quenching.

We further examined the influence of starting Pb/I stoichiometry using nominally stoichiometric, 5% PbI_2-deficient, and 5% PbI_2-rich films (Figure S5 and Table S4, Supporting Information). The nominal and PbI_2-rich films show lifetime attenuation from 29.310 to 25.355 ns and from 29.684

View Article Online
DOI: 10.1039/D6EL00062B

to 24.457 ns, respectively, after radiation exposure. In contrast, the PbI_2-deficient film has a much shorter initial lifetime (10.504 ns) but becomes more spatially uniform after radiation and shows a slight increase to 11.346 ns. These results indicate that the thermal-radiation response is strongly influenced by the starting Pb/I stoichiometry, but not in a simple monotonic manner. The PbI_2-rich film has a relatively long initial lifetime, consistent with the commonly observed passivation effect of slight PbI_2 excess. However, it also undergoes the largest lifetime attenuation after thermal radiation exposure, suggesting that a PbI_2-rich or iodide-rich near-surface environment can remain chemically vulnerable to radiation-activated halide-loss processes under vacuum. The 5% PbI_2-deficient film behaves differently. Although its average lifetime slightly increases after radiation exposure, this should not be interpreted as beneficial passivation or improved radiation stability, because its absolute lifetime remains much lower than those of the nominal and PbI_2-rich films even after irradiation. Instead, this distinct response is best interpreted as radiation-induced homogenization of an initially heterogeneous, recombination-limited film rather than true improvement of film quality, because its absolute lifetime remains far lower than those of the nominal and PbI_2-rich films.

View Article Online
DOI: 10.1039/D6EL00062B

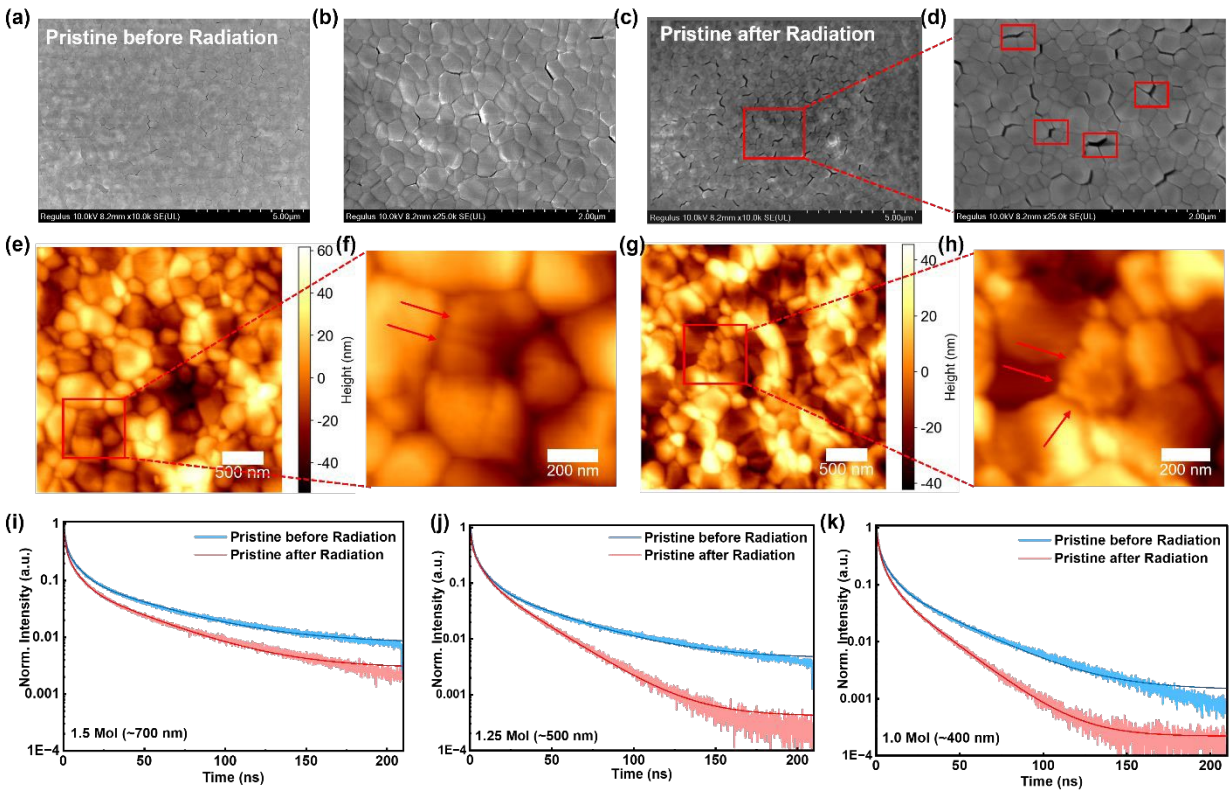

Figure 2. Radiation-induced surface morphology changes and thickness-dependent degradation. (a, b) Top-view SEM images of the pristine film before radiation at 10,000× and 25,000× magnification, respectively. **(c, d)** Top-view SEM images after 30 min of thermal-radiation exposure. **(e, f)** AFM topography image of the pristine film before radiation and an enlarged view of the marked region. **(g, h)** AFM topography image of the pristine film after radiation and an enlarged view of the marked region. **(i–k)** TRPL decay curves of 1.5, 1.25, and 1.0 M perovskite films before and after 30 min of thermal-radiation exposure.

Having established that thermal radiation structurally weakens the perovskite primarily along its grain boundaries, we hypothesized that this physical deterioration is coupled with a chemical degradation process—specifically, the outgassing of iodine-containing volatile species from these vulnerable intergranular sites. To obtain direct evidence for this release, we performed an *in-situ* trapping experiment inside the evaporation chamber (**Figure 3a**). An Ag-coated stainless-steel mesh (20 mesh) was suspended 1–2 mm below the sample holder using vacuum-compatible tape. Because Ag readily captures iodine-containing species, the coated mesh served as a getter during

View Article Online
DOI: 10.1039/D6EL00062B

irradiation. After 30-min thermal radiation exposure, XPS of the mesh positioned beneath the perovskite sample shows clear I 3d signals at 619.4 eV (3d5/2) and 630.89 eV (3d3/2) (**Figure 3b**), providing direct evidence that iodine-containing species are released from the film under thermal radiation.

Taken together, these observations indicate that the observed grain-boundary widening and morphological changes are physical manifestations of a broader near-surface chemical imbalance driven by iodine loss. The most immediate consequence is a perovskite interface that is chemically distinct from the pristine perovskite surface used to build the device stack. Because this volatilization of iodine-containing species is likely triggered by the oxidation of iodide at the exposed surfaces and weakened grain boundaries, we sought a chemical strategy to suppress this redox degradation pathway. We applied L-ascorbic acid (LAA, **Figure S1a**, Supporting Information) as a post-deposition surface treatment. As a mild redox-active surface modifier, LAA is well-suited to passivate these vulnerable sites, suppressing early halide-loss chemistry during irradiation and thereby preserving both the stoichiometric and energetic integrity of the perovskite interface. No discernible I 3d signal is detected on the mesh beneath the LAA-treated sample (**Figure 3b**), confirming that the surface treatment strongly suppresses this volatilization pathway. Although the present data do not identify every transient intermediate, they clearly show that the treatment suppresses iodine volatilization and stabilizes the near-surface electronic state.

View Article Online
DOI: 10.1039/D6EL00062B

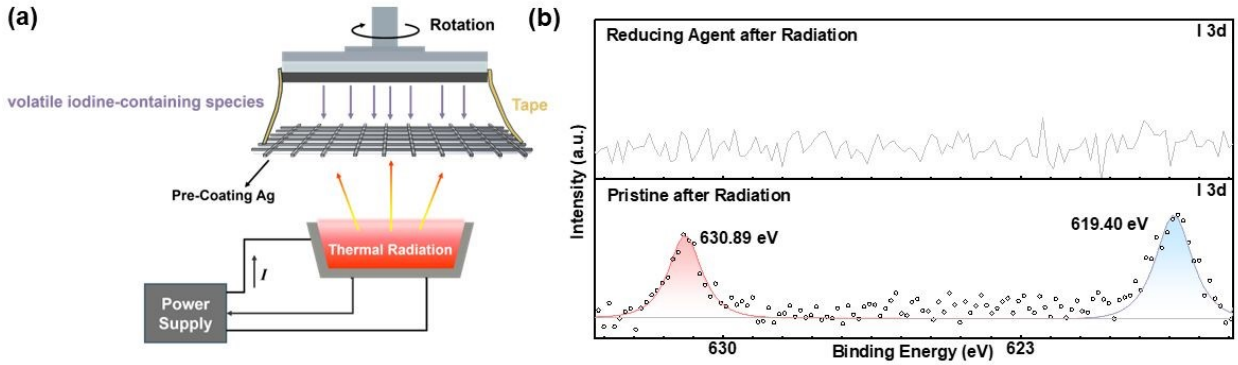

Figure 3. (**a**) Schematic illustration of the Ag-coated mesh setup used to capture volatile iodine-containing species released during thermal-radiation exposure. (**b**) High-resolution I 3d XPS spectra of the Ag-coated mesh after 30 min of exposure, comparing iodine captured from the pristine perovskite and LAA-treated perovskite samples.

Spatially resolved PL lifetime mapping (**Figure 4**) provides direct visual support for the mitigation effect of the LAA treatment. Before thermal exposure, both films exhibit relatively uniform lifetime distributions (**Figures 4a** and **4c**). After 30 min of thermal radiation, the untreated film shows pronounced lifetime quenching and broadening of the distribution (**Figure 4b**), whereas the LAA-treated film changes much less and retains a higher, more uniform lifetime response (**Figure 4d**). These results show that the surface treatment substantially suppresses, although does not completely eliminate, the degradation. This benefit also carries over to the practical evaporation step: in the PL maps after C_{60} deposition and washing off (**Figure S6**, Supporting Information), the treated films exhibit much less interfacial damage than the untreated films. The spatial contrast further supports that managing the early surface chemistry helps preserve the optoelectronic integrity of the active layer during both external irradiation tests and actual vacuum deposition.

Additional characterizations further confirm this protection. SEM images of LAA-treated films show that the surface remains compact after radiation, with no obvious radiation-induced pinholes or severe grain-boundary widening, although a small number of nanoscale particulate surface

View Article Online
DOI: 10.1039/D6EL00062B

features remain visible (Figure S7, Supporting Information). Mapping-derived lifetime fitting also shows that LAA nearly eliminates radiation-induced lifetime quenching: the PL lifetime of untreated film decreases from 29.310 to 25.355 ns, whereas the PL lifetime of the LAA-treated film essentially preserves its average lifetime from 31.176 to 31.322 ns (Figure S8 and Table S5, Supporting Information).

Notably, this mitigation is highly molecule-dependent, rather than a simple physical-overcoating effect. As summarized in **Figure S8** and **Table S5** in the **Supporting Information**, hydroquinone **(Figure S1c, Supporting Information**) and 5-methoxy-2-benzimidazolethiol (5MMBI, **Figure S1d, Supporting Information**) also preserve the average lifetime after thermal radiation, whereas D-(−)-isoascorbic acid (DIA, **Figure S1b, Supporting Information**) undergoes substantial lifetime loss, and BCP provides only partial protection (**Figure S8 and Table S5, Supporting Information**). These comparisons indicate that effective protection requires suitable interfacial chemistry and molecular compatibility, not merely the presence of an additional molecular layer.

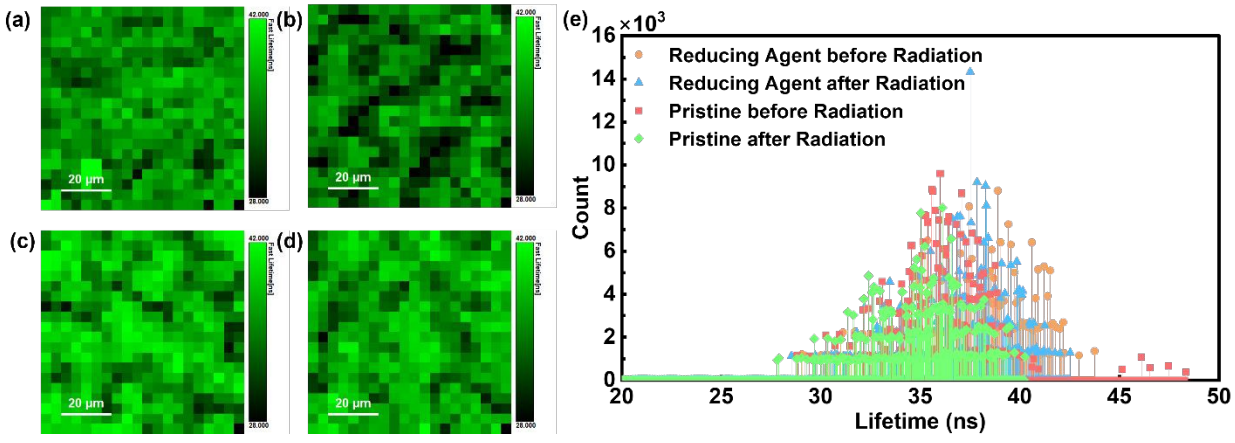

Figure 4. Spatially resolved lifetime mapping. (**a**–**d**) Spatially resolved 2D PL maps of average carrier lifetime for the pristine perovskite film (**a**, **b**) and LAA-treated (**c**, **d**) perovskite films before and after thermal-radiation exposure. (**e**) Histogram distribution of average carrier lifetimes derived from the spatially resolved 2D PL maps in panels (**a**–**d**).

View Article Online
DOI: 10.1039/D6EL00062B

To probe the chemical and electronic evolution of this structurally and chemically weakened surface, we performed X-ray photoelectron spectroscopy (XPS) on the films before and after thermal-radiation exposure. The perovskite film without LAA treatment exhibits a pronounced shift of all major core levels toward lower binding energy after irradiation. The I 3d doublet (**Figure 5a**) moves from 630.72/619.23 eV to 630.44/618.95 eV, corresponding to a shift of ~0.28 eV. The Pb 4f peaks (**Figure 5c**) shift from 143.30/138.44 eV to 143.05/138.19 eV (~0.25 eV), and the dominant FA-associated N 1s component (**Figure 5e**) shifts from 400.59 to 400.33 eV (~0.26 eV), while the MA-associated peak changes more modestly.[27] The comparable magnitude of these shifts across multiple elements is more consistent with a nearly rigid change in the surface electronic landscape than with an isolated chemical change of one species. [28] Combined with the KPFM results discussed below, these XPS shifts indicate that radiation exposure increases the surface work function and drives substantial interfacial electronic reconstruction toward a higher-work-function, more electron-deficient near-surface state. Notably, no detectable Pb^0 shoulder appears in the Pb 4f spectra, suggesting that the dominant consequence of iodine loss is not simple reduction of the lead framework. By contrast, the LAA-treated film shows only minimal spectral movement after the same exposure: the I 3d peaks shift by ~0.05 eV (**Figure 5b**), the Pb 4f peaks by ~0.04 eV (**Figure 5d**), and the FA/MA N 1s components by only ~0.04/0.03 eV (**Figure 5f**). The LAA treatment therefore strongly suppresses the chemical/electronic changes induced by thermal radiation.

View Article Online
DOI: 10.1039/D6EL00062B

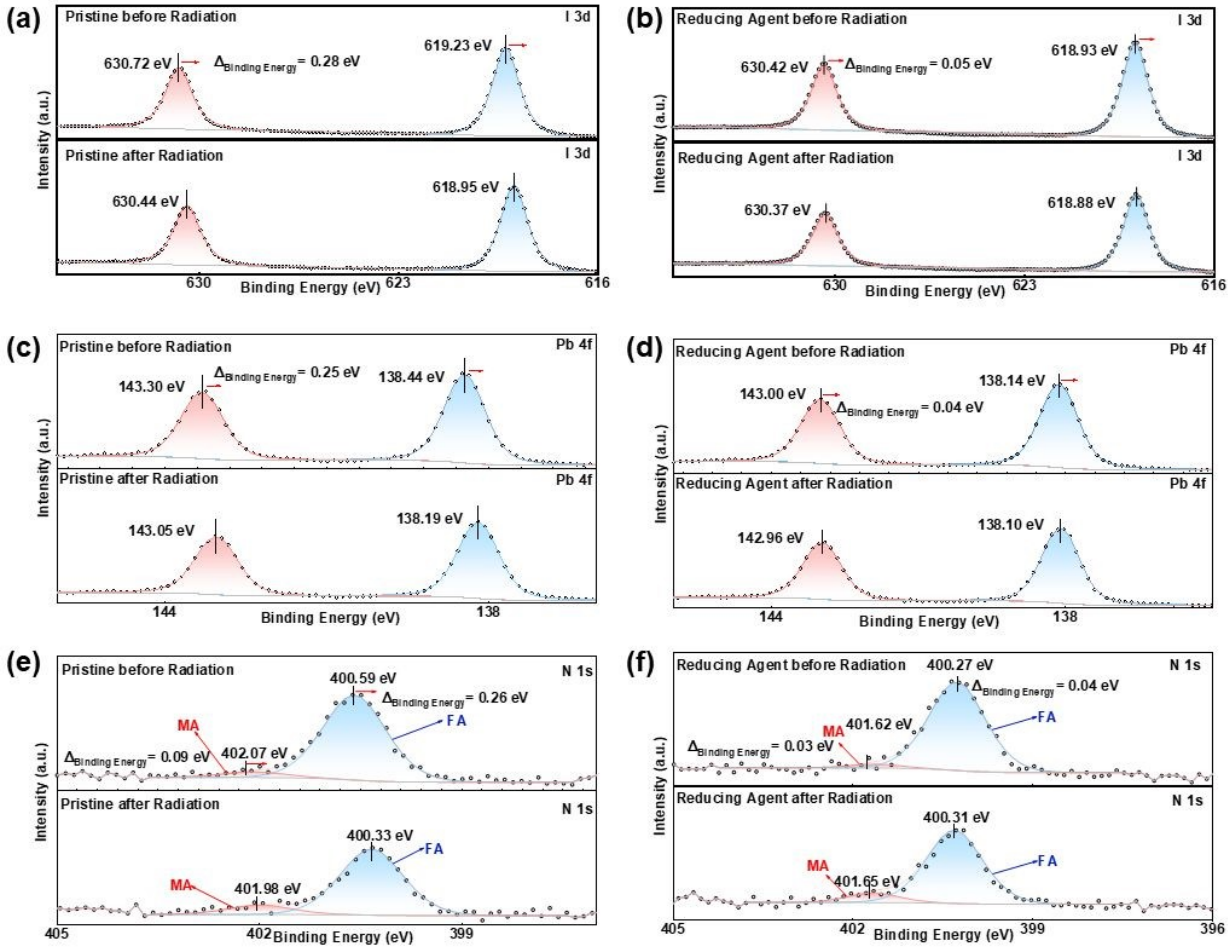

Figure 5. High-resolution XPS spectra and corresponding peak fitting results of the pristine film and reducing-agent-treated perovskite films before and after 30 min thermal-radiation exposure. (**a**) High-resolution I 3d XPS spectra of the pristine perovskite film without LAA treatment, before and after 30 min of thermal-radiation exposure. (**b**) High-resolution I 3d XPS spectra of the LAA-treated perovskite film before and after 30 min of thermal-radiation exposure. (**c**) Pb 4f spectra of the pristine film before and after radiation. (**d**) Pb 4f spectra of the reducing-agent-treated film before and after radiation. (**e**) N 1s spectra of the pristine film before and after radiation. (**f**) N 1s spectra of the reducing-agent-treated film before and after radiation.

AFM/KPFM measurements were subsequently used to correlate the surface topography with local contact potential difference (CPD) changes (**Figure 6**). The untreated film exhibits a pronounced negative shift in the overall CPD after thermal-radiation exposure, corresponding to an increased surface work function. This trend is consistent with the concerted XPS core-level shifts and supports a substantial radiation-induced modification of the near-surface electronic structure. In other words, the irradiated untreated surface becomes energetically distinct from the pristine

View Article Online
DOI: 10.1039/D6EL00062B

surface in a manner consistent with a more electron-deficient interfacial state.[29] By contrast, the LAA-treated films exhibit a distinct surface-potential evolution, suggesting that the CPD response is influenced by the LAA-rich surface layer and its radiation-induced chemical evolution. Before radiation, the fresh LAA-treated surface exhibits a highly negative CPD compared to the pristine perovskite (**Figure S10 and Note S1, Supporting Information**), indicating that the initial surface potential is influenced by the LAA-rich surface layer and its associated molecular dipole/surface-chemistry environment. After thermal-radiation exposure, however, the CPD of the LAA-treated film does not follow the pronounced negative shift observed for the untreated film. Instead, it remains much closer to that of the pristine, unexposed perovskite, indicating that the LAA treatment mitigates the radiation-induced energetic reconstruction of the perovskite surface. We therefore interpret the CPD evolution cautiously as a coupled effect of surface chemistry, molecular dipole environment, and defect formation/passivation. Consistent with this view, C 1s XPS spectra show LAA-derived oxygenated-carbon components that shift toward higher binding energy after radiation exposure (Figure S9, Supporting Information), suggesting chemical evolution of the LAA-rich surface layer during the protection of the samples from thermal radiation induced degradation.

Based on these observations, we propose a comprehensive degradation pathway: Thermal radiation induces structural widening at the grain boundaries, facilitating the escape of volatile iodine. This iodine outgassing is likely accompanied by the removal of charge-compensating organic species. Rather than leaving behind isolated donor-like iodide vacancies, this extensive localized volatilization favors an acceptor-dominant interfacial defect landscape. Such defect enrichment alters the surface termination and dipole, giving rise to a downward shift of the surface Fermi level and severely disrupting the interfacial energetic alignment—a degradation pathway

View Article Online
DOI: 10.1039/D6EL00062B

that is successfully arrested by the targeted LAA redox treatment. This chemically selective protection mechanism is consistent with the Ag-mesh/XPS trapping experiment, SEM/lifetime mapping controls, and the additional C 1s XPS evidence for radiation-induced evolution of the LAA-derived surface layer.

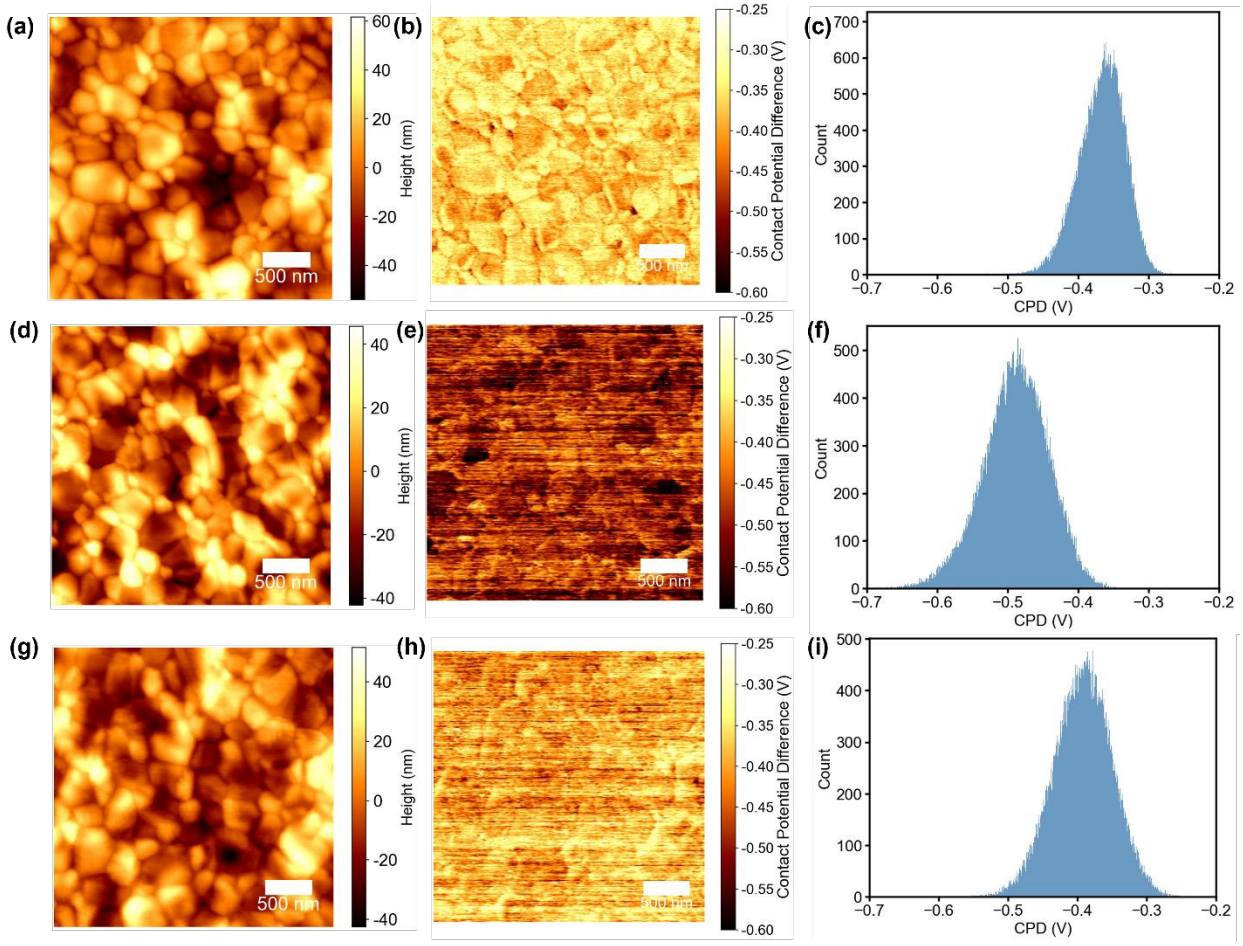

Figure 6. KPFM analysis of surface potential evolution. **(a)**, **(d)** and **(g)** AFM topography images of the pristine film before radiation, the pristine film after radiation, and the LAA-treated film after radiation, respectively. **(b)**, **(e)** and **(h)** Corresponding KPFM contact potential difference (CPD) maps of the films shown in (a), (d) and (g), respectively. **(c)**, **(f)** and **(i)** Corresponding CPD distribution histograms derived from the KPFM maps in (b), (e), and (h), respectively.

Because the radiation-induced structural widening and chemical volatilization primarily occur along the grain boundaries, we hypothesized that these defective intergranular pathways could act

View Article Online
DOI: 10.1039/D6EL00062B

as fast-diffusion channels, exacerbating ion migration throughout the entire film thickness. To determine whether this top-surface damage propagates to the buried layers, we conducted ToF-SIMS depth profiling using adjacent small pieces cut from the same parent sample before and after thermal-radiation exposure. As shown in Figure S11, the untreated film exhibits broader iodine-related signals near the buried SAM/ITO side after radiation exposure, together with a broader PO_3^- signal from the SAM region. Notably, these ToF-SIMS profiles should be interpreted qualitatively because secondary-ion intensities and sputtering behavior can depend on local matrix composition and morphology. Nevertheless, the relative comparison suggests that radiation-induced top-surface degradation is correlated with enhanced ionic redistribution near the buried interface. In contrast, the LAA-treated film shows more confined I^- and PO_3^- distributions before and after radiation exposure, consistent with suppressed radiation-induced interfacial ion redistribution.

Having established that the LAA surface treatment suppresses radiation-induced grain-boundary degradation and the ensuing ion migration, we next assessed its impact on device performance. As summarized in **Figure 7**, the untreated devices—particularly those subjected to thermal radiation—show the largest losses in open-circuit voltage (V_{oc}) and fill factor (*FF*), whereas short-circuit current (J_{sc}) changes are more modest. This pattern directly corroborates our mechanistic findings: the structural widening and iodine outgassing at the grain boundaries create electron-deficient defect states that severely increase non-radiative recombination (reducing V_{oc}), while the resulting energetic misalignment and disrupted interfacial contacts impair charge extraction (reducing *FF*). In contrast, by chemically passivating these intergranular sites, the LAA-treated devices consistently show higher median values and narrower parameter distributions, indicating both performance improvement and better reproducibility. The champion LAA-treated device

View Article Online
DOI: 10.1039/D6EL00062B

(**Figure S12 and Table S6**, Supporting Information) reaches a PCE of 20.34%, with a J_{sc} of 23.23 mA/cm^2, a V_{oc} of 1.093 V, and an *FF* of 80.07%.

Beyond the initial efficiency gains, the device stability was evaluated under standardized stress conditions. **Figure S13a** in the Supporting Information shows the light-soaking behavior under continuous one-sun illumination at 25 ± 5 °C (ISOS-L-1), and **Figure S13b** (Supporting Information) shows the thermal stability of unencapsulated devices aged at 85 °C in the dark (ISOS-D-2).[30] Under both stress conditions, the untreated devices—especially those pre-exposed to thermal radiation—degrade rapidly and largely irreversibly. This is consistent with our ToF-SIMS data: once the top-surface grain boundaries are structurally opened and chemically compromised by evaporation, they serve as active conduits for continuous ion migration during operation. In contrast, the LAA-treated devices retain the highest normalized PCE throughout the 1008 h test, demonstrating that securing the grain-boundary chemistry during fabrication vastly improves long-term operational resilience.

Interestingly, the treated devices exhibit periodic performance fluctuations rather than a strictly monotonic decay during long-term testing (**Figures S13a-b**, Supporting Information), suggesting that a reversible component may coexist with the irreversible degradation processes.[31–33] To probe this secondary observation, devices at the end of the stability test were subjected to mild heating at 50 °C (**Figure S13c**). The average PCE partially recovered after this treatment. We hypothesize that this recovery is driven by thermally activated structural relaxations within the protected grain boundaries. Gentle heating likely provides the activation energy necessary for any redistributed mobile halide species to diffuse away from the interfaces, or for localized intergranular defect complexes to temporarily anneal. This suggests that alongside irreversible chemical degradation,

View Article Online
DOI: 10.1039/D6EL00062B

partially recoverable energetic rearrangements occur in the treated devices, presenting an intriguing avenue for future operational stability engineering.

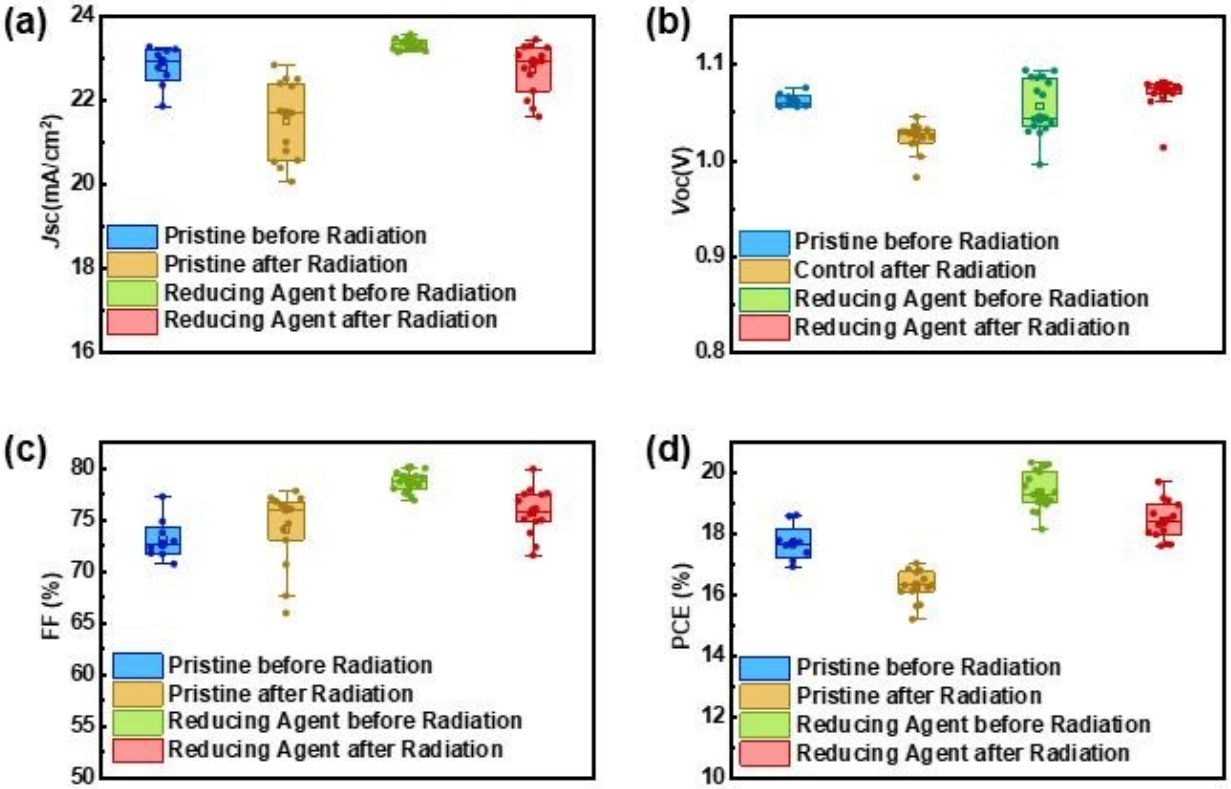

Figure 7. Comprehensive evaluation of device photovoltaic performance. **(a-d)** Statistical distributions of **(a)** current density (J_{SC}), **(b)** open-circuit voltage (V_{OC}), **(c)** fill factor (*FF*), and **(d)** power conversion efficiency (PCE) of pristine and reducing-agent-treated devices before and after radiation.

Conclusion

In summary, our results show that vacuum evaporation can act as a chemically consequential processing stage, not merely a passive route for depositing upper device layers. Under the exposure conditions used here, source-generated thermal radiation drives near-surface iodine-containing species loss, grain-boundary-localized morphological weakening, and a coupled reconstruction of the perovskite/C_{60} interfacial energetic landscape. This damage manifests primarily as V_{oc} and FF

View Article Online
DOI: 10.1039/D6EL00062B

losses, consistent with enhanced interfacial non-radiative recombination. By directly trapping iodine-containing volatile species and correlating X-ray photoelectron spectroscopy with KPFM, we move beyond simply recognizing evaporation-induced degradation to identify a chemically addressable interface-reconstruction mechanism. The L-ascorbic acid treatment suppresses this pathway and improves device robustness, highlighting perovskite-interface protection as a practical design principle for scalable inverted perovskite solar cells and related tandem-device fabrication.

METHODS

Materials

Formamidinium iodide (FAI) and methylammonium iodide (MAI) were purchased from GreatCell Materials. Lead iodide (PbI_2, 99.99%) was purchased from TCI. Cesium iodide (CsI), N,N-dimethylformamide (DMF), dimethyl sulfoxide (DMSO), isopropanol (IPA), chlorobenzene (CB), and L-ascorbic acid (anhydrous, free-flowing, ACS reagent, ≥99%) were obtained from Sigma-Aldrich. [2-(4-Methoxyphenyl)ethyl]phosphonic acid (MeO-2PACz, >99%) was purchased from Luminescence Technology Corp. (Lumtec). Fullerene (C_{60}) and bathocuproine (BCP) were purchased from Xi'an Polymer Light Technology Corp. Silver (Ag) pellets were purchased from Kurt J. Lesker. All materials were used as received without further purification.

Substrate cleaning

Glass substrates for optical characterization and patterned ITO-coated glass substrates for solar-cell fabrication and XPS measurements were sequentially cleaned in air by sonication in detergent

View Article Online
DOI: 10.1039/D6EL00062B

solution, deionized water, acetone, and isopropanol. The substrates were then treated with ozone plasma for 15 min before film deposition in an N_2-filled glovebox.

Perovskite Precursor Solution Preparation

The target perovskite composition was $FA_{0.90}MA_{0.05}Cs_{0.05}PbI_3$. The 1.5 M perovskite precursor solution was prepared by dissolving 691.5 mg PbI_2 (1.5 mmol), 232.16 mg FAI, 11.92 mg MAI, and 19.49 mg CsI in 1 mL of mixed DMF/DMSO solvent (4:1 v/v; 800 μL DMF and 200 μL DMSO). For the stoichiometry-control experiments, the PbI_2 mass was adjusted to 726 mg for the +5% PbI_2 solution and 657 mg for the -5% PbI_2 solution, while the other precursor components and solvent volume were kept the same. The solutions were stirred at room temperature until fully dissolved and filtered through a 0.45 μm PTFE filter before use.

Device Fabrication

Hole Transport Layer (HTL): The MeO-2PACz SAM solution was prepared by dissolving the powder in IPA at a concentration of 0.3 mg/mL. The SAM solution was spin-coated onto the substrate at 3000 rpm for 30 s with an acceleration of 1500 rpm/s.

Perovskite Active Layer: The perovskite films were deposited using a two-step spin-coating program: (1) 2000 rpm for 10 s (acceleration 200 rpm/s) and (2) 4000 rpm for 40 s (acceleration 1500 rpm/s). During the second step, 150 μL of CB antisolvent was dripped onto the center of the substrate at the 35th second from the start of the program. The films were then immediately annealed on a hotplate at 100 ℃ for 30 min.

Surface-modifier treatments: L-ascorbic acid (LAA), D-(−)-isoascorbic acid (DIA), hydroquinone, and 5-methoxy-2-benzimidazolethiol (5MMBI) were used as redox-active surface

View Article Online
DOI: 10.1039/D6EL00062B

modifiers, while bathocuproine (BCP) was used as a non-reducing molecular overcoating control. Each molecule was dissolved in IPA at a concentration of 0.1 mg/mL. For each treatment, 80 μL of the modifier solution was dynamically spin-coated onto the perovskite film at 3000 rpm for 30 s with an acceleration of 1500 rpm/s. For LAA, DIA, hydroquinone, and 5MMBI, the treated films were annealed at 100 °C for 10 min before subsequent characterization or device fabrication. For the BCP overcoating control, the same spin-coating procedure was used, but no post-treatment annealing was applied.

Electron Transport Layer (ETL) and Electrode: The devices were completed by thermally evaporating C_{60} (30 nm), BCP (8.5 nm), and Ag (85 nm) under vacuum. The deposition rates were controlled at 0.3 Å/s for both C_{60} and BCP, and the Ag electrode was evaporated at a rate of 0.6 Å/s.

Buffer and Contact Layer Removal: To investigate the perovskite interface buried by the thermally evaporated buffer and contact layers, the Ag electrode was mechanically peeled off using an adhesive tape. Subsequently, CB was used to wash off the C_{60} and BCP layers. Specifically, 200 μL CB was dropped onto spinning perovskite samples (3000 rpm) to dissolve and remove the C_{60} and BCP layers, exposing the underlying perovskite film.

Thermal-radiation exposure: Thermal-radiation experiments were carried out inside a vacuum chamber for 30 min. The perovskite samples were positioned approximately 12 in. (ca. 30.5 cm) above the evaporation source. For the empty-boat experiments, the chamber pressure was ~10^{-5} Pa and the Ag boat was electrically heated at 93.9 W (2.64 V, 35.6 A), matching the conditions used during Ag deposition. For comparison experiments with an Ag-loaded boat, the samples were

View Article Online
DOI: 10.1039/D6EL00062B

exposed for 30 min under the same high-vacuum conditions. The empty-boat configuration was used to reproduce the radiative load while eliminating deposited vapor species.

Characterization Methods

Solar Cell Characterization: Photovoltaic performance was evaluated by measuring current density-voltage (J-V) curves under simulated AM 1.5G illumination (100 mW/cm2). A MiniSol Sun Simulator (Model LSH-7320, Newport Corporation) was used as the light source, with the intensity calibrated using a standard silicon reference cell (Model 91150V, Newport Corporation). Data acquisition and voltage sweeps were performed using a Keithley 2400 SourceMeter Unit (SMU). The J-V curves were measured by scanning the bias from 1.5 V to 0 V in reverse scan. The active device area was defined by the evaporation shadow mask as 0.05 cm^2.

X-ray photoelectron spectroscopy (XPS) measurements were performed using a PHI Versa Probe III spectrometer equipped with a monochromatic Al Kα X-ray source (hν = 1486.6 eV). The Al anode was operated at 25 W and 15 kV, with instrument calibration performed using Au and Ag metallic binding energies. The base pressure during analysis was maintained below 1×10^{-7} Torr. The analysis area measured 500 × 500 μm^2 and was scanned using a focused beam of 100 μm in diameter. Samples were prepared by mounting on double-sided carbon adhesive tape and were subjected to dual-beam charge neutralization for charging compensation. Sample binding energies were calibrated to the C 1s peak at 284.8 eV. Survey spectra were acquired with a step size of 0.8 eV, a dwell time of 50 ms, and a pass energy of 224 eV, with three sweeps per spectrum. The C 1s spectra were obtained with three sweeps to ensure data accuracy and reproducibility.

Scanning Electron Microscopy (SEM) measurements were performed using a Hitachi SU 8230 ultra-high resolution cold-field emission scanning electron microscope.

View Article Online
DOI: 10.1039/D6EL00062B

Film Thickness Characterization: Thickness of each layer of the device was measured using KLA-Tencor Alpha-Step IQ surface profilometer.

AFM topography and KPFM measurements were performed on a commercial VERO AFM system (Asylum Research, Oxford Instruments) using a Pt/Ir coated tip (ElectriMulti75-G, Budget Sensors, stiffness ~3 N/m) in ambient atmosphere.

Time-of-flight Secondary Ion Mass Spectrometry (ToF-SIMS) measurements were performed using a TOF.SIMS5-NSC instrument (ION.TOF GmbH), using a Bi^{3+} primary ion source (30 keV energy, 0.5 nA current in DC mode, ~120 nm spot size), combined with a Cs^{+} sputter source (1 keV energy, 80 nA current in DC mode, ~10 mm spot size) and a time-of-flight mass analyzer. Characterizations were carried out in non-interlaced mode, where each scan by the primary ion beam (100 x 100 μm, ~1 s) was followed by 2 s of Cs sputtering (300 x 300 μm). For comparisons before and after thermal radiation, adjacent small pieces cut from the same parent sample were used to minimize sample-to-sample variation.

PL lifetime characterization: Time-resolved PL measurements for iodide-based perovskites were taken using a EXCELITAS photon counting module and Micro Time 100 time resolved fluorescence microscope (PICO QUANT). The samples were excited by a pulsed laser diode (Sepia PDL 828) with a center wavelength of 482 nm and a pulse rate of 0.19 MHz. The PL decay curves were fitted using a standard tri-exponential decay model to extract the carrier lifetimes:

$$I(t) = A_1\, exp\left(-\frac{t}{\tau_1}\right) + A_2\, exp\left(-\frac{t}{\tau_2}\right) + A_3\, exp\left(-\frac{t}{\tau_3}\right)$$

where I(t) is the PL intensity at time t, A_i represents the fractional amplitude of each decay component, and τ_i denotes the corresponding carrier lifetime. The average carrier lifetime (τ_{avg})

View Article Online
DOI: 10.1039/D6EL00062B

was calculated using the amplitude-weighted equation: $\tau_{avg} = \sum A_i \tau_i^2 / \sum A_i \tau_i$. For the stoichiometry and surface-modifier control experiments summarized in Tables S4 and S5, the overall PL decay was extracted by integrating photon counts over the full two-dimensional mapping area and then fitted using the same tri-exponential model.

Data Availability

Data supporting the findings of this study are available within the article (and its Supporting Information) and from the corresponding authors upon reasonable request.

Supporting Information

The Supporting Information is available online, including additional experimental details, Figures S1-S13, Tables S1-S6, and Note S1.

AUTHOR INFORMATION

Corresponding Author

Lianfeng Zhao − Holcombe Department of Electrical and Computer Engineering, Clemson University, Clemson, South Carolina 29634, United States; http://orcid.org/0000-0003-0967-6536;

Email: lianfez@clemson.edu

Notes

The authors declare no competing financial interest.

ACKNOWLEDGEMENT

View Article Online
DOI: 10.1039/D6EL00062B

The authors acknowledge support from the Clemson University Faculty Startup Fund and the National Science Foundation under Award Nos. DMR-2403802 and ECCS-2304364. This research (AFM, KPFM, and ToF-SIMS) was supported by the Center for Nanophase Materials Sciences (CNMS), which is a US Department of Energy, Office of Science User Facility at Oak Ridge National Laboratory.

References

1 N.-G. Park, H. J. Snaith and T. Miyasaka, *Nature Reviews Clean Technology 2025 2:1*, 2026, **2**, 6–7.

2 J. Jeong, M. Kim, J. Seo, H. Lu, P. Ahlawat, A. Mishra, Y. Yang, M. A. Hope, F. T. Eickemeyer, M. Kim, Y. J. Yoon, I. W. Choi, B. P. Darwich, S. J. Choi, Y. Jo, J. H. Lee, B. Walker, S. M. Zakeeruddin, L. Emsley, U. Rothlisberger, A. Hagfeldt, D. S. Kim, M. Grätzel and J. Y. Kim, *Nature 2021 592:7854*, 2021, **592**, 381–385.

3 F. Wang, S. Bai, W. Tress, A. Hagfeldt and F. Gao, *npj Flexible Electronics 2018 2:1*, 2018, **2**, 22-.

4 G. Li, Z. Zhang, B. Agyei-Tuffour, L. Wu, T. W. Gries, K. Prashanthan, A. Musiienko, J. Li, R. Zhu, L. J. F. Hart, L. Wang, Z. Li, B. Hou, M. Saba, P. R. F. Barnes, J. Nelson, P. J. Dyson, M. K. Nazeeruddin, M. Li and A. Abate, *Nature Photonics 2025 20:1*, 2025, **20**, 55–62.

5 B. Dong, M. Wei, Y. Li, Y. Yang, W. Ma, Y. Zhang, Y. Ran, M. Cui, Z. Su, Q. Fan, Z. Bi, T. Edvinsson, Z. Ding, H. Ju, S. You, S. M. Zakeeruddin, X. Li, A. Hagfeldt, M. Grätzel and Y. Liu, *Nature Energy 2024 10:3*, 2025, **10**, 342–353.

6 K. Frohna, C. Chosy, A. Al-Ashouri, F. Scheler, Y. H. Chiang, M. Dubajic, J. E. Parker, J. M. Walker, L. Zimmermann, T. A. Selby, Y. Lu, B. Roose, S. Albrecht, M. Anaya and S. D. Stranks, *Nat. Energy*, 2025, **10**, 66–76.

7 Z. Zhang, H. Wang, T. J. Jacobsson and J. Luo, *Nat. Commun.*, 2022, **13**, 7639.

8 N. Li, X. Niu, Q. Chen and H. Zhou, *Chem. Soc. Rev.*, 2020, **49**, 8235–8286.

9 N. K. Kim, Y. H. Min, S. Noh, E. Cho, G. Jeong, M. Joo, S. W. Ahn, J. S. Lee, S. Kim, K. Ihm, H. Ahn, Y. Kang, H. S. Lee and D. Kim, *Sci. Rep.*, 2017, **7**, 4645.

View Article Online
DOI: 10.1039/D6EL00062B

10 Y. A. Olanrewaju, K. Orisekeh, O. V. Oyelade, R. K. Koech, R. Ichwani, A. I. Ebunu, D. I. Amune, A. Bello, V. C. Anye, O. K. Oyewole and W. O. Soboyejo, *AIP Adv.*, 2022, **12**, 15122.

11 M. H. Miah, M. B. Rahman, M. Nur-E-Alam, M. A. Islam, M. Shahinuzzaman, M. R. Rahman, M. H. Ullah and M. U. Khandaker, *RSC Adv.*, 2025, **15**, 628–654.

12 R. Witteck, D. Nguyen Minh, G. Paul, S. P. Harvey, X. Zheng, Q. Jiang, M. Chen, T. Abzieher, A. F. Palmstrom, B. Habersberger, E. A. Gaulding, J. M. Luther and L. M. Wheeler, *ACS Appl. Energy Mater.*, 2024, **7**, 10750–10757.

13 M. Shirayama, M. Kato, T. Miyadera, T. Sugita, T. Fujiseki, S. Hara, H. Kadowaki, D. Murata, M. Chikamatsu and H. Fujiwara, *J. Appl. Phys.*, DOI:10.1063/1.4943638.

14 P. C. Huang, T. J. Yang, C. J. Lin, M. Y. Wang and W. C. Lin, *Langmuir*, 2024, **40**, 11873.

15 I. S. Zhidkov, A. I. Poteryaev, A. I. Kukharenko, L. D. Finkelstein, S. O. Cholakh, A. F. Akbulatov, P. A. Troshin, C. C. Chueh and E. Z. Kurmaev, *Journal of Physics Condensed Matter*, DOI:10.1088/1361-648X/ab576f.

16 C. Besleaga, L. E. Abramiuc, V. Stancu, A. G. Tomulescu, M. Sima, L. Trinca, N. Plugaru, L. Pintilie, G. A. Nemnes, M. Iliescu, H. G. Svavarsson, A. Manolescu and I. Pintilie, *Journal of Physical Chemistry Letters*, 2016, **7**, 5168–5175.

17 X. Ci, X. Jiang, G. Pan, K. Sun, A. Buyan-Arivjikh, Z. Li, L. Li, T. Baier, M. Schwartzkopf, S. Koyiloth Vayalil and P. Müller-Buschbaum, *Small*, 2026, **22**, e13081.

18 J. Hu, Z. Xu, T. L. Murrey, I. Pelczer, A. Kahn, J. Schwartz and B. P. Rand, *Advanced Materials*, 2023, **35**, 2303373.

19 K. K. Bhowmik, D. Ma, B. Topper, K. Koehler, S. H. Foulger, H. Xiao, L. Zhu and L. Zhao, *ACS Nano*, 2025, **19**, 38428–38439.

20 Y. Jiang, S. C. Yang, Q. Jeangros, S. Pisoni, T. Moser, S. Buecheler, A. N. Tiwari and F. Fu, *Joule*, 2020, **4**, 1087–1103.

21 M. Wang, C. Fei, M. A. Uddin and J. Huang, *Sci. Adv.*, 2022, **8**, 5977.

22 B. Kang, B. Koo, H. J. Park, W. Kim, Y. Yoo, J. Kim, S. Bae, M. J. Ko, P. Lee and H. Jung, *Adv. Energy Mater.*, 2026, **16**, e03429.

23 M. Wang, Z. Shi, C. Fei, Z. J. D. Deng, G. Yang, S. P. Dunfield, D. P. Fenning and J. Huang, *Nature Energy* |, 2023, **8**, 1229–1239.

View Article Online
DOI: 10.1039/D6EL00062B

24 C. Xiao, Z. Li, H. Guthrey, J. Moseley, Y. Yang, S. Wozny, H. Moutinho, B. To, J. J. Berry, B. Gorman, Y. Yan, K. Zhu and M. Al-Jassim, *Journal of Physical Chemistry C*, 2015, **119**, 26904–26911.

25 H. Yuan, E. Debroye, K. Janssen, H. Naiki, C. Steuwe, G. Lu, M. Moris, E. Orgiu, H. Uji-I, F. De Schryver, P. Samorì, J. Hofkens and M. Roeffaers, *Journal of Physical Chemistry Letters*, 2016, **7**, 561–566.

26 S. Du, J. Yang, S. Qu, Z. Lan, T. Sun, Y. Dong, Z. Shang, D. Liu, Y. Yang, L. Yan, X. Wang, H. Huang, J. Ji, P. Cui, Y. Li and M. Li, *Materials 2022, Vol. 15, Page 3185*, 2022, **15**, 3185.

27 G. Al-Dainy, F. Watanabe, A. S. Biris and S. E. Bourdo, *ACS Appl. Energy Mater.*, 2021, **4**, 3297–3309.

28 G. Greczynski and L. Hultman, *Nature Reviews Materials 2024 10:1*, 2024, **10**, 62–78.

29 F. Li, X. Deng, Z. Shi, S. Wu, Z. Zeng, D. Wang, Y. Li, F. Qi, Z. Zhang, Z. Yang, S. H. Jang, F. R. Lin, S. -W Tsang, X. K. Chen and A. K. Y. Jen, *Nature Photonics 2023 17:6*, 2023, **17**, 478–484.

30 M. V. Khenkin, E. A. Katz, A. Abate, G. Bardizza, J. J. Berry, C. Brabec, F. Brunetti, V. Bulović, Q. Burlingame, A. Di Carlo, R. Cheacharoen, Y. B. Cheng, A. Colsmann, S. Cros, K. Domanski, M. Dusza, C. J. Fell, S. R. Forrest, Y. Galagan, D. Di Girolamo, M. Grätzel, A. Hagfeldt, E. von Hauff, H. Hoppe, J. Kettle, H. Köbler, M. S. Leite, S. (Frank) Liu, Y. L. Loo, J. M. Luther, C. Q. Ma, M. Madsen, M. Manceau, M. Matheron, M. McGehee, R. Meitzner, M. K. Nazeeruddin, A. F. Nogueira, Ç. Odabaşı, A. Osherov, N. G. Park, M. O. Reese, F. De Rossi, M. Saliba, U. S. Schubert, H. J. Snaith, S. D. Stranks, W. Tress, P. A. Troshin, V. Turkovic, S. Veenstra, I. Visoly-Fisher, A. Walsh, T. Watson, H. Xie, R. Yıldırım, S. M. Zakeeruddin, K. Zhu and M. Lira-Cantu, *Nature Energy 2020 5:1*, 2020, **5**, 35–49.

31 W. Nie, J.-C. Blancon, A. J. Neukirch, K. Appavoo, H. Tsai, M. Chhowalla, M. A. Alam, M. Y. Sfeir, C. Katan, J. Even, S. Tretiak, J. J. Crochet, G. Gupta and A. D. Mohite, DOI:10.1038/ncomms11574.

32 W.-T. Wang, P. Holzhey, N. Zhou, Q. Zhang, S. Zhou, E. A. Duijnstee, K. J. Rietwyk, J.-Y. Lin, Y. Mu, Y. Zhang, U. Bach, C.-G. Wu, H.-L. Yip, H. J. Snaith and S.-P. Feng, *Nature* |, DOI:10.1038/s41586-024-07705-5.

33 X. Ren, J. Wang, Y. Lin, Y. Wang, H. Xie, H. Huang, B. Yang, Y. Yan, Y. Gao, J. He, J. Huang and Y. Yuan, *Nature Materials* |, 2024, **23**, 810–817.

View Article Online
DOI: 10.1039/D6EL00062B

Data Availability

Data supporting the findings of this study are available within the article (and its Supporting Information) and from the corresponding authors upon reasonable request.